



ELSEVIER

Contents lists available at ScienceDirect

Applied Mathematical Modelling

journal homepage: www.elsevier.com/locate/apm

Flow of a nanofluid in the microspacing within co-rotating discs of a Tesla turbine

Sayantan Sengupta*, Abhijit Guha¹

Mechanical Engineering Department, Indian Institute of Technology Kharagpur, Kharagpur 721302, India

ARTICLE INFO

Article history:

Received 12 February 2014

Received in revised form 21 April 2015

Accepted 13 May 2015

Available online 21 June 2015

Keywords:

Tesla disc turbine

Micro-scale flow

Rotating flow

Nanofluid

CFD simulation

Co-rotating discs

ABSTRACT

This article presents, for the first time, the fluid dynamics of the rotating flow of a nanofluid through the narrow spacings within co-rotating discs of a Tesla turbine. The inter-disc-spacing of multiple concentric discs of a Tesla disc turbine is usually of the order of 100 μm . The study is conducted with the help of both mathematical analysis and computational fluid dynamic simulations. Numerical values are reported for a specific nanofluid which is a dilute solution of ferro-particles in water (maximum volume fraction considered is 0.05). The velocity field, pressure field and fluid pathlines are calculated in the three-dimensional, axi-symmetric flow domain for prescribed boundary values for the velocity components at inlet. Detailed comparisons between the analytical and computational solutions are provided. It is explained how the fluid dynamics of rotating flow within a Tesla disc turbine is influenced by the change in volume fraction of nanoparticles. The present study reveals that, with an increase in the volume fraction of nanoparticles, the pressure-drop in the radial direction increases; the tangential velocity at any point inside the computational domain tends to increase (even though its boundary value at inlet is kept fixed for each set of computation); however, the radial velocity field remains almost invariant. The present analysis shows that, with a suitable selection of the combination of geometric and flow parameters, the use of nanofluid leads to a significant improvement in the power output (the magnitude of increase would depend on the choice of nanofluid; the sample calculations show more than 30% increase in power output when the volume fraction of nanoparticles increases from 0 to 0.05). Moreover, the gain in power output is achieved without appreciably affecting the efficiency of the turbine. Indeed the present study shows that it is possible to achieve a high efficiency (a figure of 56% is included in the paper as a sample case), revealing the potential of the Tesla disc turbine to emerge as an attractive engineering product in the field of micro-turbines.

© 2015 Elsevier Inc. All rights reserved.

1. Introduction

A Nanofluid is a dilute suspension of nano-sized particles (1–100 nm) in a base fluid [1]. Nanofluids have been primarily studied for their improved thermal characteristics (such as, enhanced thermal conductivity etc.) as compared to the conventional coolants [2,3]. This has opened up their applications in a variety of fields such as, cooling of electronic components [4],

* Corresponding author.

E-mail addresses: sayantansengupta@iitkgp.ac.in (S. Sengupta), a.guha@mech.iitkgp.ernet.in (A. Guha).¹ Professor

Nomenclature

b	gap between the two discs
d_s	diameter of the particle
p	pressure
Q	volume flow rate
R	non-dimensional radius, $R \equiv r/r_i$
r	radial direction in cylindrical co-ordinate system
U	velocity of fluid in the absolute frame of reference
V	velocity of fluid in the relative frame of reference
\dot{W}	power output
z	z -direction in cylindrical co-ordinate system
Γ_{shear}	torque produced by one side of a single disc
Δp_{io}	pressure drop between inlet and outlet
ϕ	volume fraction of nanoparticle
γ	tangential speed ratio at inlet, $\gamma \equiv \bar{U}_{\theta,i}/(\Omega r_i)$
η	efficiency
μ	dynamic viscosity of working fluid
ν	kinematic viscosity of working fluid
θ	azimuthal direction in cylindrical co-ordinate system
ρ	density of working fluid
Ω	rotational speed of disc

Subscripts

bf	properties of base fluid
eff	effective properties of nanofluid
i	at rotor inlet
o	at rotor outlet
r	component along the r direction
s	properties of solid particle
z	component along the z direction
θ	component along the θ direction

Superscripts

$\bar{()}$	sectional-averaged flow variables, $\bar{X}(r) \equiv (1/b) \int_0^b X(r) dz$
------------	---

transformer cooling [5], nuclear systems cooling [6] and many more. The density of a nanofluid increases with particle loading. Both experimental investigations [7] and theoretical studies [8,9, etc.] show that the viscosity of a nanofluid depends on the volume fraction of the suspended nanoparticles and the viscosity of the base fluid. Generally, the viscosity of a nanofluid is greater than the viscosity of its base fluid [7]. Consequently, frictional resistance and pressure drop for the flow of a nanofluid are greater than those for the flow of a pure fluid. New investigations on the frictional and thermal characteristics of nanofluids [10–13] are still being reported. The consequence of using nanofluids in devices and situations, where results for traditional fluids are known, has become an important and widespread topic of current research in many areas of fluid mechanics. In this article, we have presented a new application of nanofluids, and have investigated the effects of using nanofluids on the fluid dynamics of flow through co-rotating discs and on the performance of a Tesla disc turbine. The two facts that the presence of nanoparticles increases both viscosity and density of a nanofluid, and, that the work transfer in a Tesla disc turbine depends on the viscous shear force on the disc surfaces [14], together gave rise to the germination of a central idea of the present study that the use of nanofluids might improve the performance of a Tesla disc turbine.

The Tesla disc turbine was invented by the famous scientist Nikola Tesla in 1913 [15]. Unlike a conventional bladed turbine, the rotor of a disc turbine is formed by a series of flat, parallel, co-rotating discs which are closely-spaced and attached to a central shaft. The working fluid is injected nearly tangentially to the rotor by means of one or more inlet nozzles. The injected fluid, which passes through the narrow gaps between the discs, approaches spirally towards the exhaust port located at the centre of each disc. The viscous drag force causes the rotor of the disc turbine to rotate. There is a housing surrounding the rotor, with a small radial and axial clearance.

Rice [16] described the advances up to 1991 in the study of Tesla disc turbines. Recently, Lemma et al. [17], Hoya and Guha [18] and Guha and Smiley [19] have performed detailed experiments with Tesla disc turbines. A simple but very effective technique for measuring the net power output and overall loss called the angular acceleration method is developed by Hoya and Guha [18], which is particularly useful when the angular speed is high and torque is low. Theoretical advances in Tesla disc turbines (for single-phase flow) can be found in references [14,20–22]. A systematic dimensional analysis

(providing the appropriate non-dimensional numbers for explaining and quantifying the flow physics of the rotating flow within the narrow spacings of multiple concentric discs), a similitude study (for achieving geometric, kinematic and dynamic similarity between a model and the prototype), and, the proper scaling laws for arriving at simplified conservation equations are given in reference [23].

Researchers are currently investigating the fluid flow and heat transfer characteristics of nanofluids flowing through microchannels [24–26]. However, at present, the effect of rotation on nanofluid flow through microchannels is not thoroughly studied. Currently, the field of micro-turbines is another active research area. The bladeless Tesla turbine because of its simplicity and robustness of structure, low cost and comparatively better operation at high rpm may become a very suitable candidate for future micro-turbines. The inter-disc-spacing of multiple concentric discs of a Tesla disc turbine is usually of the order of 100 μm ; such flow domains are described in [20] as cylindrical micro-channels. Hence, the study of rotating flow of nanofluids in such micro-inter-disc-spacings of a Tesla turbine establishes a connection between micro-scale flow, nanofluid flow and rotating flow. The practical relevance of the present study is that such complex fluid dynamics controls the performance of a power producing device.

The present work provides an analytical theory for the operation of a Tesla disc turbine, which has been validated by detailed computational fluid dynamic (CFD) simulations. The analytical model is developed by using the effective properties (density and viscosity) of a nanofluid. The CFD simulations have been carried out in two ways: (i) by considering the nanofluid as a two-phase mixture, (ii) by considering the nanofluid as a single-phase fluid (using effective mixture properties). The importance of the present study is two fold:

- (1) To reveal the fluid dynamics of three-dimensional, axi-symmetric rotating flow of nanofluids within the micro-scale-spacings of co-rotating discs.
- (2) To investigate the effect of nano-particle concentration on the power output and efficiency of a Tesla disc turbine.

For a power-producing device, such as the Tesla disc turbine, there are two important figures of merit: efficiency and power output. For a Tesla disc turbine operating with a single-phase fluid (such as air or water), it is found that the graphs of efficiency versus any single geometric or flow parameter (e.g. Ω , b , $\bar{U}_{r,i}$ and $\bar{U}_{\theta,i}$) exhibits the shape of an inverted bucket. Therefore, an attempt to increase the power output by changing any of these parameters beyond the point of maximum efficiency will be accompanied by a decrease in efficiency. The present paper, on the other hand, demonstrates that the use of nanofluids can significantly increase the power output of a turbine without any detrimental effect on the efficiency.

2. Mathematical theory

In this section, a mathematical theory for the rotating flow of a nanofluid within the narrow inter-disc-spacing is presented. The effective properties (density and viscosity), which are a combination of the properties of both fluid and nanoparticles are incorporated in the present theoretical model. The density of the nanofluid can be estimated as

$$\rho_{\text{eff}} = \phi\rho_s + (1 - \phi)\rho_{\text{bf}}. \quad (1)$$

A number of theoretical models are available in the literature that can be used to estimate the effective viscosity of nanofluids. Einstein [8] developed a theoretical model for very dilute isotropic suspension of rigid spherical particles in a Newtonian fluid. According to his model, the effective viscosity of the suspension (μ_{eff}) is

$$\mu_{\text{eff}} = \mu_{\text{bf}}(1 + 2.5\phi). \quad (2)$$

Batchelor [9] incorporated the effect of the Brownian motion of the particles in a statistically homogeneous suspension and developed the following correlation:

$$\mu_{\text{eff}} = \mu_{\text{bf}}(1 + 2.5\phi + 6.2\phi^2). \quad (3)$$

A unified treatment of advection–diffusion transport of particles, of any size, dispersed in a fluid medium for laminar as well as turbulent flows has been formulated and discussed thoroughly by Guha [27].

In the present analysis, the size of the particles are very small (1–100 nm), the base fluid is Newtonian, flow within the narrow inter-disc spacing of the disc turbine is laminar and the effects of electrical and Van der Waals forces between particles are not important. Hence, the effective viscosity of the nanofluid for the present analysis can be adequately predicted by using the Batchelor's model [9].

Fig. 1 shows the physical configuration showing two circular rotor discs separated axially (i.e. in the z -direction) by a distance b . The rotor inlet is situated along the periphery of the discs (i.e. at radius r_i). The rotor outlet is at the centre of the discs (at radius r_o). The continuity equation, the momentum equations and boundary conditions are written in terms of relative velocities. For this purpose the following relations between the absolute and relative velocities are used:

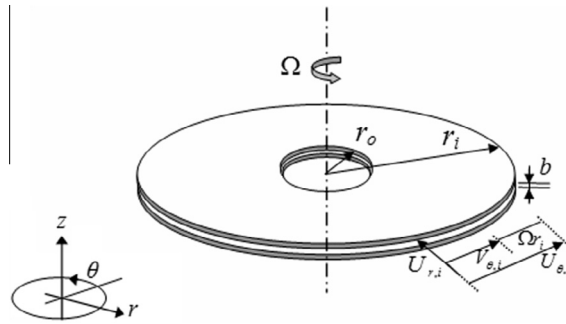


Fig. 1. Schematic diagram for the physical configuration of a Tesla disc turbine showing only two discs. (The gap within the two discs, in relation to the radius, is exaggerated in the sketch for clarity.)

$$\begin{aligned} U_r &= V_r \\ U_\theta &= (V_\theta + \Omega r) \\ U_z &= V_z \end{aligned} \quad (4)$$

The flow is assumed to be steady, laminar and axi-symmetric. Based on an order of magnitude analysis (described fully in reference [21]), the conservation equations can be consistently simplified to take the following form.

$$\text{Continuity equation} \quad \frac{\partial V_r}{\partial r} + \frac{V_r}{r} = 0 \quad (5)$$

$$\theta - \text{Momentum equation} \quad V_r \frac{\partial V_\theta}{\partial r} + \frac{V_r V_\theta}{r} + 2\Omega V_r = \nu_{\text{eff}} \frac{\partial^2 V_\theta}{\partial z^2} \quad (6)$$

$$r - \text{Momentum equation} \quad V_r \frac{\partial V_r}{\partial r} - \Omega^2 r - 2\Omega V_\theta - \frac{V_\theta^2}{r} = -\frac{1}{\rho_{\text{eff}}} \frac{dp}{dr} + \nu_{\text{eff}} \frac{\partial^2 V_r}{\partial z^2} \quad (7)$$

$$z - \text{Momentum equation} \quad \frac{\partial(p - \rho_{\text{eff}} g_z z)}{\partial z} = 0 \quad (8)$$

$$\text{Boundary conditions} \quad \text{at } r = r_i \quad \bar{V}_r = \bar{V}_{r,i}, \quad \bar{V}_\theta = \bar{V}_{\theta,i} \quad (9)$$

$$\text{at } z = 0, b \quad V_r = 0, \quad V_\theta = 0 \quad (10)$$

$$\text{at } z = b/2 \quad \frac{\partial V_r}{\partial z} = \frac{\partial V_\theta}{\partial z} = 0 \quad (11)$$

In Eqs. (5)–(8), effective mixture properties (density and viscosity) of a nanofluid are considered. The effective density (ρ_{eff}), calculated by Eq. (1), and the effective kinematic viscosity (ν_{eff}), calculated by Eq. (3), are assumed to be independent of positions for developing the analytical theory. This assumption is not imposed on the full two-phase simulations of a nanofluid as described in Section 3. A comparison of these two methods is provided in Section 4.

According to reference [21], the relative tangential and radial velocities at any radius can be expressed as

$$V_\theta(r, z) = \bar{V}_{\theta,i} \zeta(R) G(z) \quad (12)$$

$$V_r(r, z) = \bar{V}_{r,i} \zeta(R) H(z) \quad (13)$$

$$\text{where, } R = \frac{r}{r_i}, \quad \zeta(R) = \frac{\bar{V}_\theta(r)}{\bar{V}_{\theta,i}}, \quad \xi(R) = \frac{\bar{V}_r(r)}{\bar{V}_{r,i}}, \quad G(z) = \frac{V_\theta(r, z)}{\bar{V}_\theta(r)} \quad \text{and} \quad H(z) = \frac{V_r(r, z)}{\bar{V}_r(r)} \quad (14)$$

For the purpose of non-dimensional representation of the tangential and radial velocities, sectional average values of the respective quantities are used as the non-dimensionalizing parameters denoted by the symbol overbar. Thus, in Eqs. (12)–(14), $\bar{V}_\theta(r)$ is defined as $\bar{V}_\theta(r) = (1/b) \int_0^b V_\theta dz$ and $\bar{V}_r(r) = (1/b) \int_0^b V_r dz$. $\bar{V}_{\theta,i}$ is the value of $\bar{V}_\theta(r)$ at the inlet, i.e. at $r = r_i$. Similarly, $\bar{V}_{r,i}$ is the value of $\bar{V}_r(r)$ at the inlet, i.e. at $r = r_i$. R , defined in Eq. (14), is the non-dimensional radius. The r -variation of

relative tangential velocity V_θ and radial velocity V_r are incorporated in ζ and ξ , respectively. G and H are respectively the variation of V_θ and V_r within the boundary layers. Here we assume that the velocity profile is parabolic in nature. The reasons behind the above assumptions are clarified in Appendix A (also see [21]).

Accordingly, G and H are as expressed as,

$$G = H = 6 \frac{Z}{b} \left(1 - \frac{Z}{b}\right). \quad (15)$$

$\xi(R)$ is calculated by the integration of continuity equation [21]:

$$\xi(R) = \frac{\bar{V}_r(r)}{\bar{V}_{r,i}} = \frac{r_i}{r}. \quad (16)$$

According to the prediction of this analytical theory $\zeta(R)$ can be expressed as [21]:

$$\zeta(R) = \frac{\bar{V}_\theta(r)}{\bar{V}_{\theta,i}} = \left[\frac{C_2/C_1 + (1 - C_2/C_1) \exp \left\{ C_1(1 - R^2)/2 \right\}}{R} \right]$$

where, $C_1 = \frac{10v_{eff}r_i}{\bar{V}_{r,i}b^2}$ and $C_2 = \frac{-10}{6(\gamma - 1)}$. (17)

The closed-form expression for torque produced by one side of a single disc of a Tesla turbine is as follows:

$$\Gamma_{shear} = \frac{12\pi\mu_{eff}\bar{V}_{\theta,i}r_i^3}{b} \left[\frac{C_2}{2C_1}(1 - R_o^2) - \frac{(1 - C_2/C_1)}{C_1} \left\{ 1 - \exp \left[\frac{C_1}{2}(1 - R_o^2) \right] \right\} \right] \quad (18)$$

The power output due to viscous drag for the fluid flow between two successive discs can be expressed as $\dot{W} = 2\Gamma_{shear}\Omega$. In reality, a Tesla turbine consists of multiple discs. The total power output of a rotor consisting of n discs is given by:

$$\dot{W} = 2(n - 1)\Gamma_{shear} \Omega. \quad (19)$$

For single-phase flow (air as working fluid), the mathematical model (which yields a closed form solution) was validated with the experimental data given by Lemma et al. [17]. The detail of this validation is available in reference [21]. A systematic dimensional analysis (providing the appropriate non-dimensional numbers for explaining and quantifying the flow physics of the rotating flow within the narrow spacings of multiple concentric discs), a similitude study (for achieving geometric, kinematic and dynamic similarity between a model and the prototype), the proper scaling laws for obtaining Eqs. (5)–(8) from Navier–Stokes equations, and, the physical interpretation of C_1 and C_2 of Eq. (17) are given in reference [23]. It is shown that $C_1 = -10/Ds$, where $Ds (\equiv |\bar{U}_{r,i}|b^2/vr_i)$ is a new non-dimensional quantity introduced in [23] and the term “dynamic similarity number” has been coined to describe this variable. Seven non-dimensional numbers of importance have been identified for a Tesla disc turbine: (i) radius ratio ($\equiv r_o/r_i$), (ii) aspect ratio ($\equiv b/r_i$), (iii) tangential speed ratio at inlet ($\equiv \bar{U}_{\theta,i}/\Omega r_i$), (iv) flow angle at inlet ($\equiv \tan^{-1}(|\bar{U}_{r,i}|/\bar{U}_{\theta,i})$) (which is same as the nozzle angle), (v) dynamic similarity number Ds , (vi) power coefficient ($\equiv \dot{W}/(\rho|\bar{U}_{r,i}|^3r_i^2)$), and, (vii) pressure-drop coefficient ($\equiv (p_i - p_o)/(\rho\bar{U}_{\theta,i}^2)$).

3. Computational fluid dynamic simulation

A water based nanofluid (a mixture of water and ferro-particles) is chosen as the working medium. Present CFD simulations have been performed for various inlet volume fractions (in the range of 0%–5%) of nanoparticles. Two different sets of CFD simulations are carried out in the present study. In the first set of computations, nanofluids are considered as two-phase mixtures. Complete two-phase flow simulations are therefore carried out. In these simulations, the properties of both water and ferro-particles, and, the diameter of the particles are to be specified. In the second set of computations, effective mixture properties (density and dynamic viscosity) are used to represent the properties of nanofluids; and, single-phase CFD simulations are performed. In this approach, the diameter of the nanoparticles does not need to be specified. Although, the two-phase simulations give more accurate representations for nanofluid-flow, the two-phase simulations require much more computational time as compared to the single-phase simulations. Both two-phase and single-phase simulations are compared with the analytical solutions.

Unless otherwise stated, the diameter of the ferro-particles (d_s) and the density of the ferro-particles (ρ_s) considered here are 20 nm and 8030 kg/m³, respectively. For one set of computations, in which the effect of the diameter of the nanoparticles on the turbine performance is studied, the diameter of nanoparticles is varied between 5 nm to 100 nm.

The two-phase flow (many aspects of two-phase flow are given in [28–30]) of a nanofluid is solved by the mixture model [31]. The mixture model is an Eulerian–Eulerian method for solving multi-phase flow. Akbari et al. [32] showed that the velocity field for a nanofluid flow can be predicted with a reasonable accuracy by the mixture model. Ungarish [33] and

Wu et al. [34] used the mixture model to predict rotational flow. The conservation equations of this model for steady and laminar flow [31] are as given below.

$$\text{Continuity equation : } \nabla \cdot (\rho_m \vec{U}_m) = 0 \quad (20)$$

$$\text{Momentum equation : } \nabla \cdot (\rho_m \vec{U}_m \vec{U}_m) = -\nabla p_m + \nabla \cdot \vec{\tau}_m + \nabla \cdot \vec{\tau}_{Dm} + \rho_m \vec{g} \quad (21)$$

$$\text{Volume fraction equation : } \nabla \cdot (\rho_s \phi_s \vec{U}_m) = -\nabla \cdot (\rho_s \phi_s \vec{U}_{dr,s}) \quad (22)$$

In Eq. (21), ρ_m ($\rho_m \equiv \sum_{k=1}^n \phi_k \rho_k$) is the density of the mixture; \vec{U}_m ($\vec{U}_m \equiv \frac{1}{\rho_m} \sum_{k=1}^n \phi_k \rho_k \vec{U}_k$) is the velocity of the mixture; $\vec{\tau}_m$ ($\vec{\tau}_m \equiv \sum_{k=1}^n \phi_k \vec{\tau}_k$) is the average viscous stress tensor and $\vec{\tau}_{Dm}$ ($\vec{\tau}_{Dm} \equiv \sum_{k=1}^n \phi_k \rho_k \vec{U}_{dr,k} \vec{U}_{dr,k}$) is the diffusion stress tensor due to phase slip. $\vec{U}_{dr,k}$ ($\vec{U}_{dr,k} \equiv \vec{U}_k - \vec{U}_m$) is the drift velocity of phase k relative to the centre of the mixture mass. In the present study, the number of phases n is 2. Water is considered as the primary phase and nanoparticles are considered as the secondary phase. Volume fraction equation is solved only for the secondary phase (which is represented by the subscript s in Eq. (22)). The relative velocity of the particles with respect to water is calculated from the equation of slip proposed by Manninen et al. [31]. The equation of slip velocity $\Delta \vec{U}$ is as follows:

$$\Delta \vec{U} = (\vec{U}_s - \vec{U}_{bf}) = \frac{\tau_s}{(C_D Re_s / 24)} \frac{(\rho_s - \rho_m)}{\rho_s} \vec{a}_s \quad (23)$$

where, \vec{a}_s is the particle's acceleration, τ_s ($\tau_s \equiv \rho_s d_s^2 / 18 \mu_{bf}$) is the particle relaxation time and C_D is the drag coefficient. The following expression, proposed by Schiller and Naumann [35], is used here to calculate C_D

$$C_D = 24 / Re_s (1 + 0.15 Re_s^{0.687}) \quad Re_s \leq 1000 \\ = 0.44 \quad Re_s > 1000 \quad (24)$$

where, Re_s ($Re_s \equiv \frac{d_s |\Delta \vec{U}|}{\nu_{bf}}$) is the particle Reynolds number.

A commercially available CFD software Fluent 6.3.26 is utilised for the present computation. A three dimensional, double precision, pressure based, steady and implicit solver is used. Velocity formulation is in the absolute frame of reference and flow is considered to be laminar (a discussion regarding the transition from laminar to turbulence within the inter-disc-spacing of a Tesla disc turbine is provided in [14,22]; the flow remains laminar if the dynamic similarity number Ds is less than 10; the value of Ds used in the present study is much less than 10). The SIMPLE algorithm, with second order upwind scheme for momentum and the 'Standard' scheme (pressure on the control-faces being obtained through interpolation of their corresponding cell-centre pressure values) for discretizing the pressure equation, is utilised.

The QUICK scheme (Quadratic Upstream Interpolation for Convective Kinematics) is employed for solving the volume fraction equation, which is third-order accurate according to its originator [36]. Fluent offers two options for computing the value of a convected variable at a face: first order upwind and the QUICK scheme. For achieving higher order accuracy in the spatial discretization of the volume fraction, the QUICK scheme is selected for the computations reported in the present paper. QUICK-type schemes are based on a weighted average of second-order-upwind and central interpolations of the convected variable.

The geometry of the computational domain (Fig. 1) and the grid in the cylindrical co-ordinate system (in the r , θ and z directions) are generated by the commercially available software GAMBIT 2.4.6. The flow within two successive discs, separated by a small gap (b), is considered. Each disc has an inlet radius (r_i) and an outlet radius (r_o). At inlet, a parabolic distribution is specified for both tangential and radial components of velocity (the sensitivity of the velocity distribution at inlet is assessed in Appendix A). The z -component of velocity at the inlet is zero. The outlet boundary condition is modelled by the 'pressure outlet' option offered by Fluent, with zero gauge pressure. No slip boundary condition is set on the disc walls. A rotational speed (Ω) of the disc is also set. The details for the geometry and the boundary conditions used for the present study are given in Table 1.

For the boundary conditions reported in this paper, the fluid flow field is axi-symmetric. However, our ultimate aim is to understand the flow physics comprehensively, this includes non-uniform inlet and exit boundary conditions, for example to reflect the presence of one or more discrete nozzles placed circumferentially at the inlet. It is also interesting to study the three-dimensional fluid pathlines. It may also be possible to uncover whether there may arise any flow instabilities in the

Table 1
Geometry and boundary conditions.

Geometry	Boundary conditions		
Inlet radius (r_i)	25 mm	At inlet	$\vec{U}_r = -0.5$ m/s; $\vec{U}_\theta = 5$ m/s; $U_z = 0$ m/s (Velocity distribution is parabolic, Eq. (15))
Outlet radius (r_o)	13.2 mm	At outlet	$p = 101325$ Pa
Inter-disc-spacing (b)	0.13 mm	On disc surfaces	$\Omega = 150$ rad/s

Table 2Grid independence test. (for water as working fluid, $\phi = 0$).

Grid Distribution	Number of grids in r , θ and z directions	Total number of cells	Δp_{io} (Pa)
Coarse	(50 \times 95 \times 30)	142,500	13,296
Standard	(100 \times 190 \times 60)	1,140,000	13,310
Fine	(150 \times 285 \times 90)	3,847,500	13,312

θ -direction even if the geometry and boundary conditions are axi-symmetric. Since computational resources or CPU time did not pose any constraint for the present problem, we therefore adopted the generic methodology for the solution of three-dimensional flow field since non-uniform boundary conditions can be introduced when required.

A systematic method is employed to select an appropriate convergence criterion. For this, CFD iterations with a given geometry and boundary conditions are progressed up to three different levels of convergence; in each run the maximum 'scaled' residual [37] for all conserved variables (i.e., mass, velocity components and volume fraction of nanoparticles) is set at a particular value, the three values used in the three runs being 10^{-9} , 10^{-10} and 10^{-11} . It is found that when the maximum 'scaled' residual is changed from 10^{-10} to 10^{-11} , the corresponding change in Δp_{io} (which is an integrated output parameter) is less than 0.00001%. Hence, a maximum 'scaled' residual of 10^{-10} is chosen as the convergence criterion for the present study. Each CFD simulation took about 32 h to converge in an OptiPlex 990 desktop system with 8 GB RAM and 64-bit, 3.1 GHZ core i5 processor.

A grid-independence test has been carried out (Table 2 showing a few pertinent details), and based on this study, a total of 1,140,000 (100 \times 190 \times 60) mapped, hexahedral computational cells are used for the results presented below. Among several output parameters, Δp_{io} , for its relatively high sensitivity with the change in the number of computational cells, is chosen as a testing parameter to determine the optimum number of cells. Table 2 shows the computed values of Δp_{io} for three different grid distributions (coarse, standard and fine). While increasing the number of cells simultaneously in the r , θ and z directions, it has been observed that, the computed value of Δp_{io} varies until a grid distribution of 100 \times 190 \times 60, which corresponds to a total of 1,140,000 computational cells, is attained. However, any further increase in the number of computational cells in the r , θ and z directions leads to a marginal change of Δp_{io} (e.g., the computed value of Δp_{io} for 3,847,500 cells differs marginally from the computed value of Δp_{io} for 1,140,000 cells; see Table 2).

4. Results and discussion

In this section, the results obtained from the analytical theory (Section 2) and that from CFD simulations (Section 3) are presented and compared. It is to be remembered that the CFD simulations have been carried out in two ways: (i) by considering the nanofluid as a mixture of two separate phases, (ii) by considering the nanofluid as a single-phase fluid (using effective mixture properties). Some important fluid dynamic aspects of the rotating flow of a nanofluid within the narrow inter-disc-spacings and their consequences on the performance of a Tesla disc turbine have been explained below.

Table 3 shows the effective values of properties (density, dynamic viscosity and kinematic viscosity) of a nanofluid for various volume fractions (ϕ) of nanoparticles at inlet. The effective property values are needed for the analytical theory and for the single-phase CFD simulations. Eqs. (1) and (3), which are used to calculate respectively the effective density (ρ_{eff}) and effective dynamic viscosity (μ_{eff}) of the nanofluid, imply that ρ_{eff} and μ_{eff} increase with an increase in ϕ . However, the effective kinematic viscosity (ν_{eff}), which is the ratio of effective dynamic viscosity (μ_{eff}) to effective density (ρ_{eff}), decreases with increase in ϕ . The consequences of the decrease in ν_{eff} with an increase in ϕ are discussed later.

Table 3 also shows the power output (\dot{W}) for the flow of nanofluid between two successive co-rotating discs. The power output (\dot{W}) for various values of ϕ is calculated analytically by using Eqs. (18) and (19), and, computationally by using CFD simulations. CFD results from both single-phase and two-phase simulations are included. The geometry and the boundary

Table 3

Effective properties of nanofluid and amount of power output derived from nanofluid flow for various volume fractions of nanoparticles.

Volume fraction ϕ of particles	Effective Density ρ_{eff} (kg/m ³) of nanofluid (Eq. (1))	Effective dynamic viscosity μ_{eff} (Pa.s) of nanofluid (Eq. (3))	Effective kinematic viscosity, ν_{eff} (m ² /s), of nanofluid	Power output \dot{W} (W)		
				From two-phase CFD simulation	From single-phase CFD simulation	From analytical solution (Eqs. (18) and (19))
0	997	1.003×10^{-3}	1.006×10^{-6}	0.149	0.149	0.151
0.01	1067.33	1.029×10^{-3}	0.964×10^{-6}	0.159	0.159	0.161
0.02	1137.66	1.056×10^{-3}	0.928×10^{-6}	0.168	0.169	0.171
0.03	1207.99	1.084×10^{-3}	0.897×10^{-6}	0.177	0.179	0.181
0.04	1278.32	1.113×10^{-3}	0.871×10^{-6}	0.186	0.189	0.192
0.05	1348.65	1.144×10^{-3}	0.848×10^{-6}	0.195	0.199	0.202

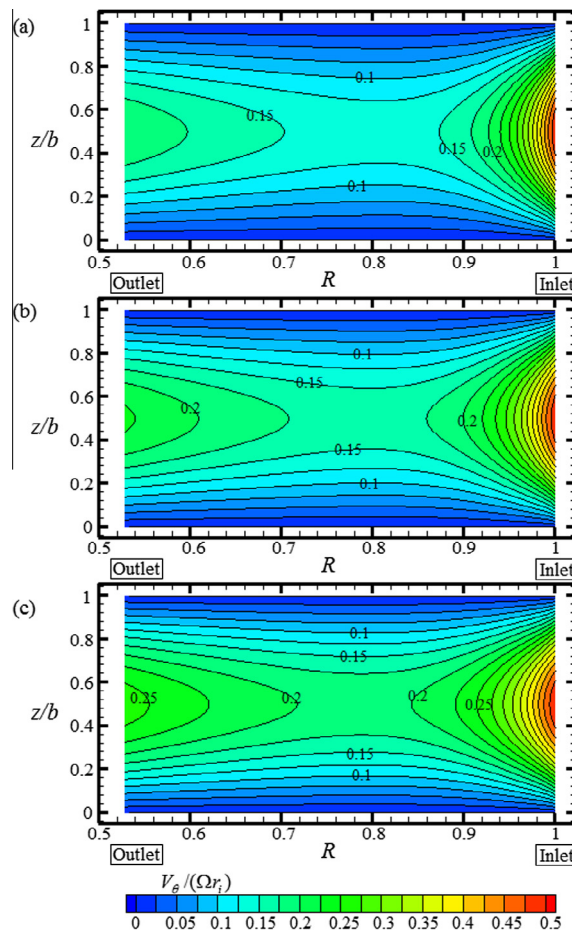


Fig. 2. (colour online) Contour for non-dimensional relative tangential velocity $V_\theta/(\Omega r_i)$ of nanofluids on a rz plane as obtained from the present CFD simulations. (a) for $\phi = 0$ (single-phase simulation); (b) for $\phi = 0.02$ (two-phase simulation); (c) for $\phi = 0.04$ (two-phase simulation).

conditions required for calculating \dot{W} are given in Table 1. Table 3 shows that \dot{W} obtained from analytical solutions agree well with \dot{W} obtained from CFD simulations. It can be observed that even when $\phi = 0.05$, the difference between the results of the present analytical theory and that obtained from the rigorous and computationally expensive two-phase CFD solutions is only 3.6%. This demonstrates the utility of the analytical theory developed here.

Figs. 2–4 show respectively the contours of non-dimensional relative tangential velocity $V_\theta/(\Omega r_i)$, non-dimensional absolute tangential velocity $U_\theta/(\Omega r_i)$ and absolute value (modulus) of non-dimensional radial velocity $|U_r|/|\bar{U}_{r,i}|$ obtained from the present two-phase CFD simulations (the method of non-dimensionalization is given in [23]). The geometry and the boundary conditions required for these computations are given in Table 1. The velocity fields are axi-symmetric because axi-symmetric boundary conditions are applied at both inlet and outlet. Hence, the contours are shown on a rz plane. For no slip boundary condition on the disc-surfaces (at $z/b = 0$ and $z/b = 1$), $V_\theta/(\Omega r_i)$ in Fig. 2 and $|U_r|/|\bar{U}_{r,i}|$ in Fig. 4 are zero; and, $U_\theta/(\Omega r_i)$ in Fig. 3 is equal to 1. It can be observed that V_θ (Fig. 2), U_θ (Fig. 3) and $|U_r|$ (Fig. 4) increase from the disc-surfaces and obtain a maximum value at the middle of the disc spacing (at $z/b = 0.5$). The z -variations of both V_θ and U_θ have important implications concerning the power output \dot{W} of a Tesla turbine. The values of \dot{W} depends on $(\partial U_\theta/\partial z)_{z=0,b}$ or $(\partial V_\theta/\partial z)_{z=0,b}$. The shapes and values of the contour lines in Figs. 2 and 3 indicate that $(\partial U_\theta/\partial z)_{z=0,b}$ and $(\partial V_\theta/\partial z)_{z=0,b}$ are non-zero and that work is transferred from the fluid to the disc surfaces. It can be inferred from Eqs. (17)–(19) that \dot{W} depends on γ ($\gamma \equiv \bar{U}_{\theta,i}/(\Omega r_i)$). Figs. 2–4 represent the cases corresponding to $\gamma = 1.33$, i.e. when γ is greater than 1. When the value of γ is less than 1, new physics involving flow reversal arises. A detailed discussion on the work transfer within a Tesla disc turbine is given in reference [14].

Figs. 2–4 also show the r -variation of non-dimensional V_θ , non-dimensional U_θ and non-dimensional $|U_r|$, respectively. It can be seen from Fig. 2 that, with a decrease of r from r_i ($R = 1$), V_θ decreases to a minimum value at a certain radius and then onwards increases. A similar trend can also be obtained from Eq. (17) which gives the radial variation for sectional-averaged relative tangential velocity \bar{V}_θ . Eq. (17) shows that the radial variation of \bar{V}_θ depends on the value of γ . Most of the results of

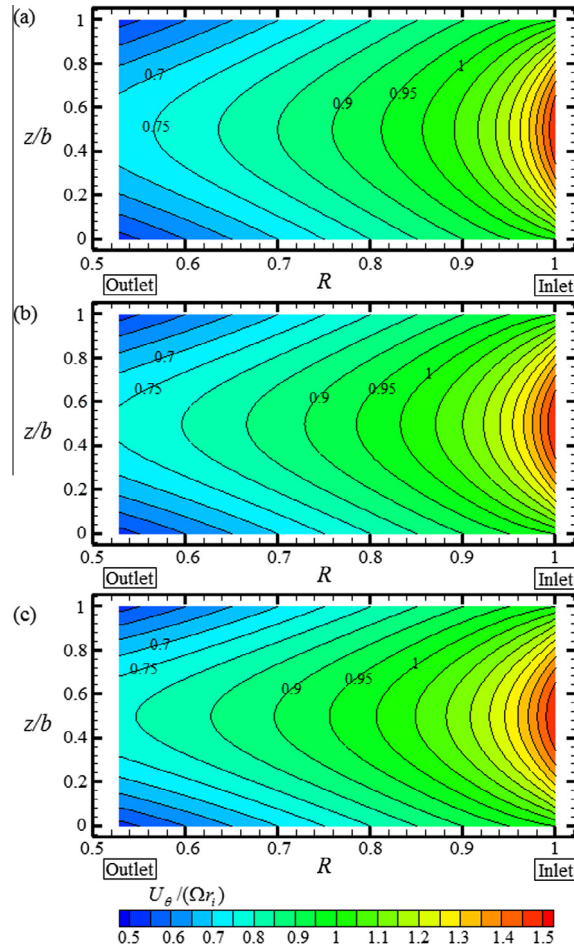


Fig. 3. (colour online) Contour for non-dimensional absolute tangential velocity $U_\theta/(\Omega r_i)$ of nanofluids on a rz plane as obtained from the present CFD simulations. (a) for $\phi = 0$ (single-phase simulation); (b) for $\phi = 0.02$ (two-phase simulation); (c) for $\phi = 0.04$ (two-phase simulation).

this paper are shown for a particular value of γ i.e., for $\gamma = 1.33$. Guha and Sengupta [22] had shown the radial variation of \bar{V}_θ for various values of γ . Reference [22] includes many interesting flow phenomena (such as, flow reversal) which can be explained only with respect to a relative frame of reference. These subject matters are not discussed here for the brevity of the present article. Fig. 3 shows that U_θ decreases from inlet to outlet. U_θ depends on both V_θ and Ωr (Eq. (4)). Within a short radial distance from the inlet, U_θ decreases rapidly because of the rapid decrease of V_θ and the linear decrease of Ωr . After attaining a minimum value, V_θ increases towards the outlet. As a result, the rate of decrease of U_θ is reduced. If the chosen outlet radius is sufficiently small, an increase of U_θ towards the outlet can be captured [14]. Such increase of U_θ happens when the effect of increase in V_θ overtakes the effect of decrease in Ωr . Fig. 4 shows that $|U_r|$ progressively increases in the r -direction towards the outlet. It is so because the flow area ($2\pi r b$) decreases gradually with a decrease in r ; and, the fluid flow (steady, incompressible and axi-symmetric) has to satisfy the equation of continuity.

Figs. 2–4 also reveal the effect of change in ϕ respectively on V_θ , U_θ and $|U_r|$. It can be observed from Figs. 2–4 that both V_θ and U_θ (Figs. 2 and 3) are sensitive to the change in ϕ though $|U_r|$ (Fig. 4) remains almost insensitive to the change in ϕ . The above observation can be explained from the analytical theory. Substituting Eqs. (15) and (17) into Eq. (12), it can be shown that V_θ depends on the viscosity and density of the fluid. Eq. (4) shows that U_θ is a function of V_θ and therefore, U_θ depends on the fluid properties. However, Eqs. (13), (15) and (16) show that $|U_r|$ does not depend on the fluid properties (viscosity and density). Thus, $|U_r|$ varies negligibly with respect to ϕ .

Figs. 2a, 2b and 2c show respectively the contours of non-dimensional V_θ for $\phi = 0$, $\phi = 0.02$ and $\phi = 0.04$. It can be seen from Figs. 2a, 2b and 2c that V_θ , starting from the same value at the inlet, decreases at a faster rate for lower values of ϕ . At the outlet, the value of V_θ is greater for higher values of ϕ .

Guha and Sengupta [22] explained that the change of \bar{V}_θ in the radial direction depends on the relative magnitude of various forces. In θ -momentum equation (Eq. (6)), $2\Omega V_r$ is the θ -component of Coriolis acceleration; $\frac{V_r V_\theta}{r}$ takes an important part

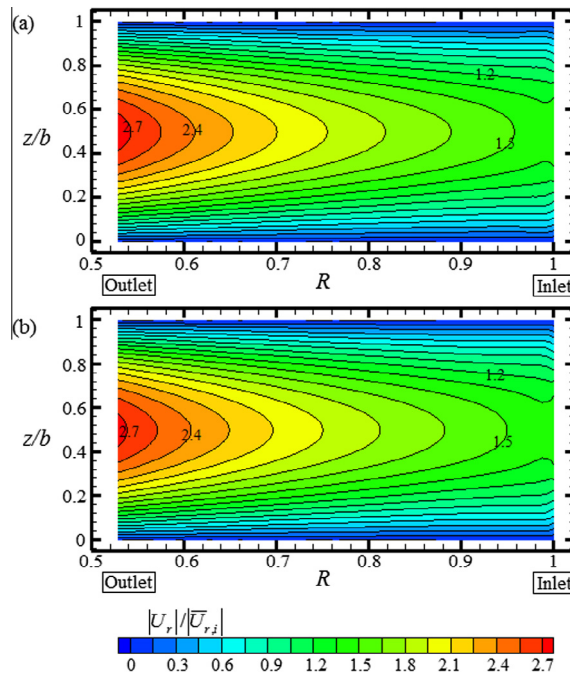


Fig. 4. (colour online) Contour for (the absolute value of) non-dimensional radial velocity ($|U_r|/|\bar{U}_{r,i}|$) of nanofluids on a rz plane as obtained from the present CFD simulations. (a) for $\phi = 0$ (single-phase simulation); (b) for $\phi = 0.02$ (two-phase simulation).

to conserve the angular momentum of the working fluid; and, $v_{eff} \frac{\partial^2 V_\theta}{\partial z^2}$ represents the viscous (frictional) acceleration. Eq. (6) can be expressed in the following form:

$$-\frac{\partial V_\theta}{\partial r} = \frac{V_\theta}{r} + 2\Omega - \frac{v_{eff}}{V_r} \frac{\partial^2 V_\theta}{\partial z^2}$$

Eq. (25) may be interpreted as a relation that specifies the value of $(-\partial V_\theta / \partial r)$, i.e. how V_θ changes with respect to r in the negative r -direction (i.e., from inlet to outlet). Depending on the relative magnitudes of various accelerations, $(-\partial V_\theta / \partial r)$ may be positive, zero or negative.

Ω is always a positive quantity; therefore, the value of V_θ at $\gamma = 1.33$ is also positive in the whole flow domain (except on the disc-surfaces where is V_θ zero). Hence, both θ -component of Coriolis acceleration and $\frac{V_r V_\theta}{r}$ try to increase V_θ in the negative r -direction. On the other hand, both $\frac{\partial^2 V_\theta}{\partial z^2}$ and V_r are negative; therefore, viscous acceleration tries to decrease V_θ in the negative r -direction. These are the roles of various forces for a particular ϕ . The subject matter of the next paragraph is how the contributions of various forces vary with ϕ .

Eq. (25) shows that $(-\partial V_\theta / \partial r)$ due to the θ -component of Coriolis acceleration is independent of the kinematic viscosity of fluid (therefore, independent of ϕ). On the other hand, $(-\partial V_\theta / \partial r)$ due to both viscous acceleration and $\frac{V_r V_\theta}{r}$ depends on the kinematic viscosity of fluid. Table 1 shows that the effective kinematic viscosity of fluid v_{eff} decreases with an increase in ϕ . Attributing only to this fact, one may conclude that the contribution of viscous acceleration, in relation to $(-\partial V_\theta / \partial r)$, decreases with an increase in ϕ . This results into an increase of V_θ . Under this condition, the value of V_θ towards outlet (in the negative r -direction) may further increase due to $\frac{V_r V_\theta}{r}$ (Eq. (25)). However, the explanation is not so straight forward because the viscous acceleration also depends on $\frac{\partial^2 V_\theta}{\partial z^2}$. The magnitude of $\frac{\partial^2 V_\theta}{\partial z^2}$ ($|\frac{\partial^2 V_\theta}{\partial z^2}|$) increases for the increase in V_θ (Eqs. (12) and (15)). For the present case, however, the geometric and boundary conditions (given in Table 1) are such that the effect of decrease of v_{eff} overtakes the effect of increase of $|\frac{\partial^2 V_\theta}{\partial z^2}|$. Consequently, with increase in ϕ , an overall decrease of the term $\frac{v_{eff}}{V_r} \frac{\partial^2 V_\theta}{\partial z^2}$ occurs and, V_θ increases.

Figs. 3a, 3b and 3c show the contours of non-dimensional U_θ respectively for $\phi = 0$, $\phi = 0.02$ and $\phi = 0.04$. It can be seen from Figs. 2a, 2b and 2c that, starting from the same value at the inlet, the value of V_θ at any radius is greater for higher values of ϕ . The difference in the value of U_θ , for $\phi = 0$, $\phi = 0.02$ and $\phi = 0.04$, is clearly visible near the outlet.

Fig. 5 shows absolute pathlines which are calculated at the mid-plane ($z = b/2$) of the flow domain for various values of ϕ . It can be observed that the shape, size and orientation of absolute pathlines vary with ϕ . It has been discussed previously that the radial velocity field does not change with ϕ . Fig. 3 shows that the absolute tangential velocity increases with increase in ϕ . As a result, the length of absolute pathlines shown in Fig. 5 increases with an increase in ϕ . The orientations of absolute

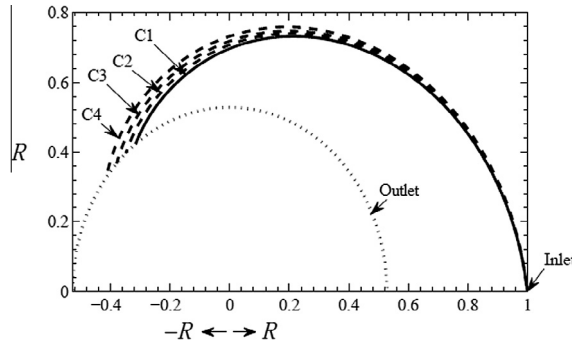


Fig. 5. Absolute pathlines of nanofluids for various particle concentrations (ϕ). [— Prediction of the present analytical model C1: for $\phi = 0$. ---- Results obtained from the present two-phase CFD simulations C2: for $\phi = 0$; C3: for $\phi = 0.02$; C4: for $\phi = 0.04$.]

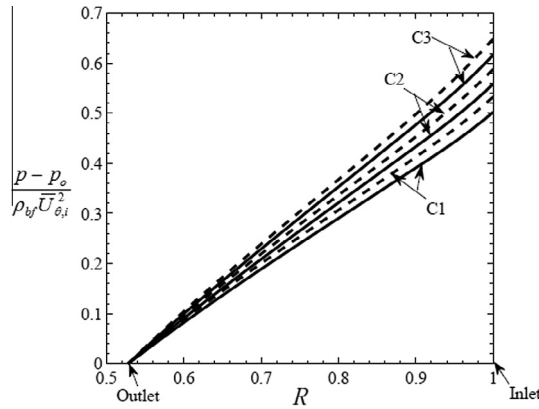


Fig. 6. Radial distribution of non-dimensional gauge pressure for nanofluids within the inter-disc-spacing of a Tesla turbine. [— Prediction of the present analytical model (which is closer to the single-phase CFD simulations not shown here for clarity); ---- Results obtained from the present two-phase CFD simulations. C1: for $\phi = 0$; C2: for $\phi = 0.02$; C3: for $\phi = 0.04$.]

pathlines are governed by the angle $\tan^{-1}(U_r/U_\theta)$. Near inlet, the orientations are same for all values of ϕ because the working fluid enters the inter-disc-spacing at an angle of $\tan^{-1}(U_{r,i}/U_{\theta,i})$ which is same for all the cases. However, near outlet, the orientations are different because U_θ depends on the properties (density and viscosity) of nanofluids. For pure fluid flow ($\phi = 0$), a comparison shows that the absolute pathline calculated from the analytical theory matches well with the absolute pathline computed from the present CFD simulation.

Fig. 6 shows the radial distribution of non-dimensional gauge pressure for the nanofluid flow between two coaxial rotating discs of a Tesla turbine. Pressure distributions for various ϕ are calculated both analytically and computationally. It can be observed from this figure that, with an increase in ϕ , pressure drop between inlet and outlet increases. To explain the reason, the r -momentum equation is expressed in the following form (by substituting Eq. (5) into Eq. (7)):

$$\frac{dp}{dr} = \rho_{eff} \left(\frac{V_\theta^2}{r} + \frac{V_r^2}{r} \right) + \rho_{eff} \Omega^2 r + 2\rho_{eff} \Omega V_\theta + \mu_{eff} \frac{\partial^2 V_r}{\partial z^2}. \tag{26}$$

Integrating Eq. (26) from inlet (r_i) to outlet (r_o), both overall pressure drop between inlet and outlet (Δp_{io}) and its components due to various forces can be estimated. $\int_{r_o}^{r_i} \rho_{eff} (V_\theta^2/r + V_r^2/r) dr$ represents pressure drop due to inertial component of force, $\int_{r_o}^{r_i} \rho_{eff} \Omega^2 r dr$ represents pressure drop due to centrifugal component of force, $\int_{r_o}^{r_i} 2\rho_{eff} \Omega V_\theta dr$ represents pressure drop due to r -component of Coriolis force and $\int_{r_o}^{r_i} \mu_{eff} \frac{\partial^2 V_r}{\partial z^2} dr$ represents pressure drop due to r -component of viscous force. Effective density (Eq. (1)) and effective viscosity (Eq. (3)) of the nanofluid increase with an increase in ϕ . It has been explained previously that the change of radial velocity field with respect to ϕ is negligible. Fig. 2 shows that the value of V_θ at any radial location increases with an increase in ϕ . Therefore, the increase of overall pressure drop as observed in Fig. 6 can be attributed to the fact that the pressure drop due to each component of force increases individually with an increase in ϕ .

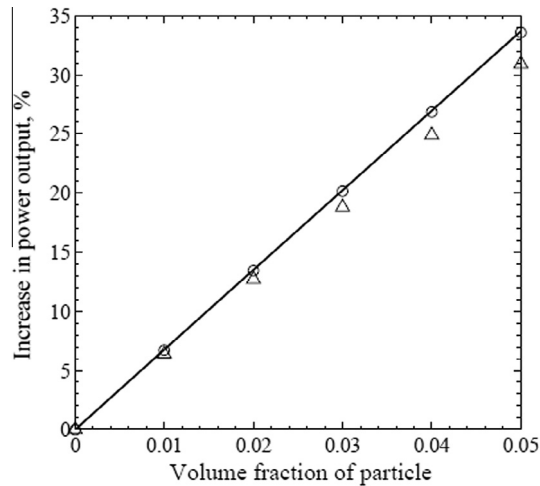


Fig. 7. Percentage of increase in power output with an increase in the volume fraction of nanoparticles in the base fluid. [Δ % increase in power output obtained from the present two-phase CFD solution; \circ % increase in power output obtained from the present single-phase CFD solution; $-$ % increase in power output obtained from the present analytical solution].

Fig. 7 shows the percent increase in power output with an increase in ϕ for three set of calculations (single-phase CFD simulations, two-phase CFD simulations and analytical solutions). Percent increase in power output is defined as $100\Delta\dot{W}/\dot{W}$ ($\Delta\dot{W}/\dot{W} \equiv (\dot{W}|_{\text{any}\phi} - \dot{W}|_{\phi=0})/\dot{W}|_{\phi=0}$). For each set of calculation, $\dot{W}|_{\phi=0}$ denotes the value of \dot{W} at $\phi = 0$ for the corresponding set. Fig. 7 shows that \dot{W} obtained from the analytical solution increases by 33.8% when ϕ increases from 0 to 0.05. Percent increase in \dot{W} is also obtained from single-phase and two-phase CFD simulations. With the analytical solutions the results of single-phase simulation match better than the results of two-phase CFD simulation. The deviation is greater for higher values of ϕ .

Eq. (19) gives the expression for power output \dot{W} . For a particular value of Ω , the increase in \dot{W} is due to the increase in Γ_{shear} . Γ_{shear} is equal to $\int_{r_0}^{r_i} \tau_w 2\pi r^2 dr$ where, τ_w is the shear stress at $z = 0$. τ_w is a product of μ_{eff} and $(\partial V_\theta/\partial z)_{z=0}$. Table 3 shows that μ_{eff} increases by 14% when ϕ increases from 0 to 0.05. Analytical solution gives that $(\partial V_\theta/\partial z)_{z=0}$ equals $6\bar{V}_\theta(r)/b$. Fig. 2 shows that, for the chosen value of inter-disc-spacing (given in Table 1), $\bar{V}_\theta(r)$ increases with an increase in ϕ . Therefore, more than 30% increase in \dot{W} is a result of the combined effect of these two factors.

The efficiency of a disc turbine was defined in various ways by the previous researchers [18]. From these, the following definition of efficiency (η) is adopted here for the numerical illustrations,

$$\eta = \frac{\dot{W}}{Q(p_i + 0.5\rho_{eff}(U_{\theta,i}^2 + U_{r,i}^2))}. \quad (27)$$

Eq. (27) is similar to that given by Roddy et al. [38] for a disc-pump. In Eq. (27), \dot{W} is the power output for fluid flow between two successive discs; Q ($= -2\pi r_i b U_{r,i}$) is the volume flow rate between two successive discs; and $(p_i + 0.5\rho_{eff}(U_{\theta,i}^2 + U_{r,i}^2))$ is the gauge value of total pressure at inlet.

Efficiency η is calculated by using Eq. (27) with the data obtained from analytical solutions, single-phase CFD simulations and two-phase CFD simulations (these calculations are performed using the geometry and boundary conditions given in Table 1). Both analytical and CFD solutions show that a high value of η can be obtained for the micro-scale rotating flow within a Tesla turbine. Within a range of ϕ from 0 to 0.05, η obtained from both single-phase and two-phase CFD simulations vary between 56% and 57%; and, η obtained from the analytical solutions vary between 59% to 60%.

Additional two-phase CFD simulations are carried out to establish the effects of varying some of the important operating parameters (such as, diameter of the nanoparticles, rotational speed of the disc, mass flow rate and inter-disc-spacing) on the performance of a Tesla disc turbine. No significant change in the performance of a Tesla disc turbine is observed while varying the diameter of the nanoparticles from 5 nm to 100 nm. The performance of a Tesla disc turbine, however, significantly depends on the other operating parameters. Table 4 shows a summary of these parametric computed results which are organised in three clusters.

Cluster 1: The effects of varying the rotational speed of the disc Ω are studied in this set of computations. The other boundary conditions and the geometry of the turbine remain the same as given in Table 1. Two representative values of Ω , 80 rad/s (less than $\Omega = 150$ rad/s, given in Table 1) and 350 rad/s (greater than $\Omega = 150$ rad/s) are selected to examine

Table 4
Effect of varying the operating parameters on the performance of the turbine.

Cluster	Fixed parameters (values same as given in Table 1)	Varying parameters	η (%) at $\phi = 0$	η (%) at $\phi = 0.05$	\dot{W} (W) at $\phi = 0$	$\Delta\dot{W}/\dot{W}$ (%) as ϕ changes from 0 to 0.05
1	$r_i, r_o, b, \bar{U}_{r,i}$ and $\bar{U}_{\theta,i}$	$\Omega = 80$ rad/s	45	46	0.099	33
		$\Omega = 150$ rad/s	56	56	0.149	31
		$\Omega = 350$ rad/s	19	16	0.100	8
2	r_i, r_o, b and Ω	$\bar{U}_{r,i} = -0.25$ m/s $\bar{U}_{\theta,i} = 2.5$ m/s	33	34	0.020	28
		$\bar{U}_{r,i} = -0.5$ m/s $\bar{U}_{\theta,i} = 5$ m/s	56	56	0.149	31
		$\bar{U}_{r,i} = -1$ m/s $\bar{U}_{\theta,i} = 10$ m/s	44	41	0.726	29
3	$r_i, r_o, \Omega, \bar{U}_{r,i}$ and $\bar{U}_{\theta,i}$	$b = 0.065$ mm	37	44	0.079	34
		$b = 0.13$ mm	56	56	0.149	31
		$b = 0.26$ mm	43	36	0.240	25

the effect of varying Ω . Table 4 shows that the values of η for both $\Omega = 80$ rad/s and $\Omega = 350$ rad/s are smaller than the values of η for $\Omega = 150$ rad/s. $\dot{W}|_{\phi=0}$ for $\Omega = 80$ rad/s and $\Omega = 350$ rad/s are also less than $\dot{W}|_{\phi=0}$ for $\Omega = 150$ rad/s. The increase in power output $\Delta\dot{W}/\dot{W}$ by using nanofluids is only 8% for $\Omega = 350$ rad/s. Thus, such a large Ω is not effective. For $\Omega = 80$ rad/s, $\Delta\dot{W}/\dot{W}$ is high (33%) though $\dot{W}|_{\phi=0}$ is small and η is not large. Thus, $\Omega = 80$ rad/s is also not a good choice.

Cluster 2: The inlet velocity components are varied to alter the mass flow rate. The geometry and Ω remain the same as given in Table 1. For an n times increase in the mass flow rate, $\bar{U}_{r,i}$ is increased by n times. $\bar{U}_{\theta,i}$ is also increased by n times to maintain the same flow angle at inlet ($\tan^{-1}(\bar{U}_{r,i}/\bar{U}_{\theta,i})$). Table 4 shows that $\dot{W}|_{\phi=0}$ increases with an increase in the mass flow rate. $\Delta\dot{W}/\dot{W}$ for $n = 0.5$ ($\bar{U}_{r,i} = -0.25$ and $\bar{U}_{\theta,i} = 2.5$) and $n = 2$ ($\bar{U}_{r,i} = -1$ and $\bar{U}_{\theta,i} = 10$) are less than $\Delta\dot{W}/\dot{W}$ for $n = 1$ (Table 1). The values of η for both $n = 2$ and $n = 0.5$ are significantly lower than those corresponding to $n = 1$. Hence, both the cases corresponding to $n = 2$ and $n = 0.5$ are not suitable for designing an effective Tesla disc turbine.

Cluster 3: The inter-disc spacing b is varied. All boundary conditions and other geometric details remain the same as given in Table 1. CFD simulations are carried out for $b = 0.26$ mm (which is two times larger than the value of b given in Table 1) and $b = 0.065$ mm (which is the half of the value given in Table 1). Table 4 shows that $\dot{W}|_{\phi=0}$ increases with b ; however, this should be analysed in the context of how many discs can be accommodated within a given overall dimension, and this allowable number of discs depend on the selected inter-disc-spacing. The values of η for both $b = 0.26$ mm and $b = 0.065$ mm are considerably smaller as compared to the value of η corresponding to $b = 0.13$ mm. Hence, a decrease of inter-disc-spacing b tends to increase the efficiency but decreasing b below a certain value may result in a significant decrease in the efficiency of a Tesla disc turbine.

In brief, for obtaining simultaneously a high value of efficiency, a sufficiently high value of power output and a large increase in power output by using nanofluids, the combination of geometric and flow parameters of a Tesla turbine needs to be selected properly.

5. Conclusion

The present paper investigates, for the first time, the consequence of using nanofluids on the flow through co-rotating discs and on the performance of a Tesla disc turbine. The fluid dynamics of the three-dimensional, axi-symmetric rotating flow of a specific nanofluid (a dilute solution of ferro-particles) within the micro-spacing of two co-rotating discs is studied both analytically and computationally. It is found that the analytical solutions agree well with the results obtained from the CFD simulations.

The present study is important from both physical and practical perspectives. It is discovered that with an increase in the volume fraction ϕ of nanoparticles, the pressure-drop in the radial direction increases; the tangential velocity at any point inside the computational domain tends to increase (even though its boundary value at inlet is kept fixed for each set of computation); however, the radial velocity field remains almost invariant. With an increase in ϕ , the length of absolute pathlines increases and the orientation of absolute pathlines changes. The reasons behind such fluid dynamic aspects have been analysed by the mathematical theory.

For a power-producing device, such as the Tesla disc turbine, there are two important figures of merit: efficiency and power output. For a Tesla disc turbine operating with a single-phase fluid (such as air or water), it is found that the graphs of efficiency versus any single geometric or flow parameter (e.g. Ω , b , $\bar{U}_{r,i}$ and $\bar{U}_{\theta,i}$) exhibits the shape of an inverted bucket. Therefore, an attempt to increase the power output by changing any of these parameters beyond the point of maximum efficiency will be accompanied by a decrease in efficiency. The present paper, on the other hand,

demonstrates (see Table 4) that the use of nanofluids can significantly increase the power output of a turbine without any detrimental effect on the efficiency. The sample calculations for a specific nanofluid consisting of water and ferro-particles shown in Fig. 7 reveal that more than 30% increase in power output can be obtained by increasing ϕ from 0 to 0.05. Moreover, the gain in power output is achieved without appreciably affecting the efficiency of the turbine. Indeed the present study shows that it is possible to achieve a high value of efficiency (as an example, a value of 56% is shown in Table 4) for micro-scale rotating flow within a Tesla disc turbine. This performance for a rotor of such a small size indicates that the Tesla disc turbine can emerge as an attractive engineering product in the field of micro-turbines.

It is shown that a high value of efficiency, a sufficiently high value of power output and a large increase in power output by using nanofluids can be realised simultaneously, only when the selection of the geometric and flow parameters is appropriate.

Acknowledgement

Shubham Choudhary, while pursuing his final year B.Tech.-project under A.G. (one of the authors of this paper), had performed some computations regarding an earlier version of this work.

Appendix A

The rationale behind the choice of Eq. (15)

In Section 2, Eq. (15) represents parabolic distributions corresponding to the z -variations of V_θ and V_r (G and H) within the inter-disc-spacing of a Tesla turbine. Velocity distributions can also be calculated by post-processing the data obtained from the full two-phase flow CFD simulations (Section 3). In this Section, a comparison is provided between G and H obtained from the two-phase flow CFD simulations and the expressions for G and H as given by Eq. (15).

Fig. A.1 shows a representative computation for $\phi = 2\%$ (geometry and boundary conditions used for the present computation are taken from Table 1). It can be observed that G and H of the mixture (nanofluid) obtained from the two-phase CFD simulations at $R = 0.6$ agree well with the expressions for G and H as given by Eq. (15). A 2.7% maximum deviation for H and a 4% maximum deviation for G are found at $z/b = 0.5$. If the single-phase CFD simulation is used instead of the two-phase simulation, the agreement in the value of H is better; however, such results are not included in Fig. A.1 for the sake of clarity.

An accurate calculation of power output depends on an accurate estimation of $(\partial V_\theta / \partial z)_{z=0}$. Fig. A.1 shows that near the disc surfaces, the predictions of Eq. (15) are in close agreement with the velocity profiles obtained from the CFD simulations.

Sensitivity of the boundary condition for velocity at inlet

In Section 3, parabolic velocity distributions are specified at the inlet boundary of the computational domain. Guha and Sengupta [14] have shown that a uniform velocity distribution at inlet develops to a parabolic distribution within a short radial span from the inlet. In this section, the integrated output quantities of the CFD simulations (\dot{W} and Δp_{io}) corresponding

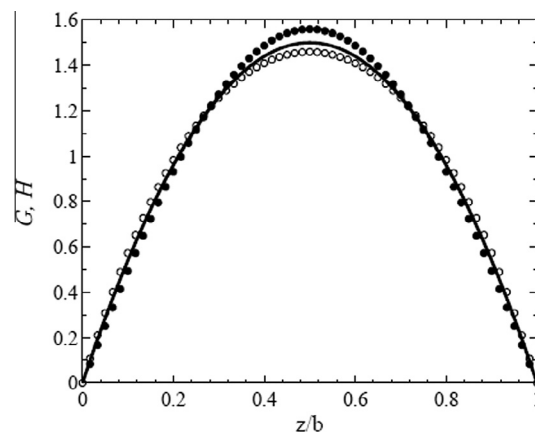


Fig. A.1. A comparison between G and H of the mixture (nanofluid) obtained from two-phase CFD simulations and the expressions of G and H as given by Eq. (15). [— Eq. (15); ● G obtained from two-phase CFD simulation for $\phi = 2\%$ at $R = 0.6$; ○ H obtained from two-phase CFD simulation for $\phi = 2\%$ at $R = 0.6$].

to uniform velocity distributions at inlet are compared with that corresponding to parabolic velocity distributions at inlet. Thus, the sensitivity of parabolic distributions at inlet is assessed here. Example calculations for two-phase CFD simulations with $\phi = 2\%$ are performed for both uniform and parabolic distributions at inlet. Geometry and boundary conditions (other than the velocity distributions at inlet) for these computations are the same as given in Table 1. For both uniform and parabolic distributions, the sectional-averaged velocity components at the inlet are the same as given in Table 1. The simulations corresponding to these two distributions show 0.14% deviation in Δp_{i0} and 4.8% deviation in \dot{W} (deviations are calculated with respect to parabolic distributions at inlet). In reality, the velocity distributions at the inlet of the inter-disc-spacing may be neither uniform nor parabolic. An intermediate choice between these two distributions (uniform and parabolic) may rather be more appropriate. It is, however, difficult to measure experimentally the velocity distribution at inlet of the inter-disc-spacing. Considering such difficulties and accounting the small deviations (as given above) for the integrated output parameters, a parabolic velocity profile is selected as an engineering approximation.

References

- [1] J.H. Lee, K.S. Hwang, S.P. Jang, B.H. Lee, J.H. Kim, S.U.S. Choi, C.J. Choi, Effective viscosities and thermal conductivities of aqueous nanofluids containing low volume concentrations of Al_2O_3 nanoparticles, *Int. J. Heat Mass Transfer* 51 (11–12) (2008) 2651–2656.
- [2] J.A. Eastman, U.S. Choi, S. Li, L.J. Thompson, S. Lee, Enhanced thermal conductivity through the development of nanofluids, *Materl. Res. Soc. Proc.* 457 (1996) 3–11.
- [3] Y. Hwang, H.S. Park, J.K. Lee, W.H. Jung, Thermal conductivity and lubrication characteristics of nanofluids, *Curr. Appl. Phys.* 6 (S1) (2006) 67–71.
- [4] P. Naphon, S. Klangchart, S. Wongwises, Numerical investigation on the heat transfer and flow in the mini-fin heat sink for CPU, *Int. Commun. Heat Mass Transfer* 36 (8) (2009) 834–840.
- [5] C. Choi, H.S. Yoo, J.M. Oh, Preparation and heat transfer properties of nanoparticle-in-transformer oil dispersions as advanced energy-efficient coolants, *Curr. Appl. Phys.* 8 (6) (2008) 710–712.
- [6] R. Saidur, K.Y. Leong, H.A. Mohammad, A review on applications and challenges of nanofluids, *Renew. Sustain. Energy Rev.* 15 (3) (2011) 1646–1668.
- [7] B.C. Pak, Y.I. Cho, Hydrodynamic and heat transfer study of dispersed fluids with submicron metallic oxide particles, *Exp. Heat Transfer* 11 (2) (1998) 151–170.
- [8] A. Einstein, A new determination of molecular dimensions, *Ann. Phys.* 19 (1906) 289–306 (and 34, 591–592) [Einstein, A. 1906 Eine neue Bestimmung der Moleküldimensionen. *Annalen der Physik*, 324(2), 289–306].
- [9] G.K. Batchelor, The effect of Brownian motion on the bulk stress in the suspension of spherical particles, *J. Fluid Mech.* 83 (1) (1977) 97–117.
- [10] C.C. Tang, S. Tiwari, M.W. Cox, Viscosity and friction factor of aluminum oxide-water nanofluid flow in circular tubes, *J. Nanotechnol. Eng. Med.* 4 (2) (2013) 021004.
- [11] C. Hu, M. Bai, J. Lv, P. Wang, X. Li, Molecular dynamics simulation on the friction properties of nanofluids confined by idealized surfaces, *Tribol. Int.* 78 (2014) 152–159.
- [12] M.A. Hachey, C.T. Nguyen, N. Galanis, C.V. Popa, Experimental investigation of Al_2O_3 nanofluids thermal properties and rheology—effects of transient and steady-state heat exposure, *Int. J. Therm. Sci.* 76 (2014) 155–167.
- [13] P. Chandrasekaran, M. Cheralathan, V. Kumaresan, R. Velraj, Enhanced heat transfer characteristics of water based copper oxide nanofluid PCM (phase change material) in a spherical capsule during solidification for energy efficient cool thermal storage system, *Energy* 72 (2014) 636–642.
- [14] A. Guha, S. Sengupta, The fluid dynamics of work transfer in the non-uniform viscous rotating flow within a Tesla disc turbomachine, *Phys. Fluids* 26 (3) (2014) 1–27. 033601.
- [15] N. Tesla, Turbine, US Pat. 1,061,206, 1913.
- [16] W. Rice, Tesla turbomachinery, in: E. Logan (Ed.), *Handbook of Turbomachinery*, Marcel Dekker, New York, 2003, pp. 861–874.
- [17] E. Lemma, R.T. Deam, D. Toncich, R. Collins, Characterisation of a small viscous flow turbine, *J. Exp. Therm. Fluid Sci.* 33 (2008) 96–105.
- [18] G.P. Hoya, A. Guha, The design of a test rig and study of the performance and efficiency of a Tesla disc turbine, *Proc. Inst. Mech. Eng. Part A: J. Power Energy* 223 (A4) (2009) 451–465.
- [19] A. Guha, B. Smiley, Experiment and analysis for an improved design of the inlet and nozzle in Tesla disc turbines, *Proc. Inst. Mech. Eng. Part A: J. Power Energy* 224 (2010) 261–277.
- [20] V.D. Romanin, V.P. Carey, An integral perturbation model of flow and momentum transport in rotating microchannel with smooth or microstructured wall surfaces, *Phys. Fluids* 23 (8) (2011). Art no. 082003.
- [21] S. Sengupta, A. Guha, A theory of Tesla disc turbines, *Proc. Inst. Mech. Eng. Part A: J. Power Energy* 226 (5) (2012) 650–663.
- [22] A. Guha, S. Sengupta, The fluid dynamics of the rotating flow in a Tesla disc turbine, *Eur. J. Mech. B. Fluids* 37 (2013) 112–123.
- [23] A. Guha, S. Sengupta, Similitude and scaling laws for the rotating flow between concentric discs, *Proc. Inst. Mech. Eng. Part A: J. Power Energy* 228 (4) (2014) 429–439.
- [24] J. Chevalier, O. Tillement, F. Ayela, Rheological properties of nanofluids flowing through microchannels, *Appl. Phys. Lett.* 91 (23) (2007). 233103(1–3).
- [25] J. Li, C. Kleinstreuer, Thermal performance of nanofluid flow in microchannels, *Int. J. Heat Fluid Flow* 29 (4) (2008) 1221–1232.
- [26] J.Y. Jung, H.S. Oh, H.Y. Kwak, Forced convective heat transfer of nanofluids in microchannels, *Int. J. Heat Mass Transfer* 52 (1–2) (2009) 466–472.
- [27] A. Guha, Transport and deposition of particles in turbulent and laminar flow, *Annu. Rev. Fluid Mech.* 40 (2008) 311–341.
- [28] A. Guha, Computation, analysis and theory of two-phase flows, *Aeronaut. J.* 102 (1012) (1998) 71–82.
- [29] A. Guha, A unified theory for the interpretation of total pressure and temperature in two-phase flows at subsonic and supersonic speeds, *Proc. R. Soc. A: Math. Phys. Eng. Sci.* 454 (1998) 671–695.
- [30] Y. Mei, A. Guha, Implicit numerical simulation of transonic flow through turbine cascades on unstructured grids, *Proc. Inst. Mech. Eng. Part A: J. Power Energy* 219 (2005) 35–47.
- [31] M. Manninen, V. Taivassalo, S. Kallio, On the Mixture Model for Multiphase Flow, VTT Publications 288 (1996) 3–67.
- [32] M. Akbari, N. Galanis, A. Behzadmehr, Comparative analysis of single and two-phase models for CFD studies of nanofluid heat transfer, *Int. J. Therm. Sci.* 50 (2011) 1343–1354.
- [33] M. Ungarish, On the modeling and investigation of polydispersed rotating suspensions, *Int. J. Multiphase Flow* 21 (2) (1995) 267–284.
- [34] Y. Wu, S. Liu, H.S. Dou, L. Zhang, Simulations of unsteady cavitating turbulent flow in a Francis turbine using the RANS method and the improved mixture model of two-phase flows, *Eng. Comput.* 27 (3) (2011) 235–250.
- [35] L. Schiller, A. Naumann, Über die grundlegenden Berechnungen bei der Schwerkraftaufbereitung, *Z. Ver. Dtsch. Ing.* 77 (1933) 318–320.
- [36] B.P. Leonard, S. Mokhtari, ULTRA-SHARP nonoscillatory convection schemes for high-speed steady multidimensional flow. NASA TM 1–2568 (ICOMP-90-12), NASA Lewis Research Center, 1990
- [37] *Fluent 6.3 User's Guide 2006*. Fluent Inc., Central Source Park, 10 Cavendish Court, Lebanon, NH 03766, USA.
- [38] P.J. Roddy, R. Darby, G.L. Morrison, P.E. Jenkins, Performance characteristics of a multipledisk centrifugal pump, *J. Fluids Eng.* 109 (1987) 51–57.